

**Resolving Multi-stage Rupture Process of the 2021 M_w 4.9 Offshore Jeju Island
Earthquake from Relative Source Time Functions**

Sangwoo Han¹, Won-Young Kim², Hobin Lim³, Young Oh Son¹, Min-Seong Seo¹,
Jun Yong Park¹, and YoungHee Kim^{1*}

¹ School of Earth and Environmental Sciences, Seoul National University, Seoul, Republic of Korea

² Lamont-Doherty Earth Observatory of Columbia University, NY, USA

³ Earthquake Research Center, Korea Institute of Geoscience and Mineral Resources, Daejeon, Republic of
Korea

Contents of this file

Texts S1 to S7
Figures S1 to S10
Table S1

Introduction

The supporting information provides additional details of procedures performed in this study and addresses the implications of using the time window that includes the origin times of both target and EGF events when retrieving RSTFs. Analyses for estimating moment ratios between subevents, calculating static shear stress perturbation, and determining subevent locations and origin times from the Lg -wave RSTFs are described. Lastly, the dispersion effect of Lg wave on the RSTFs is discussed. One table and ten figures are appended in this file.

Text S1. Construction of origin-time preserved RSTFs

The RSTFs used in this study are obtained by aligning the waveforms of the EGF event and target event (mainshock) on the same travel-time window starting from the origin times of each event, instead of aligning on the phase arrival times (e.g., López-Comino and Cesca, 2018; Wu et al., 2019) or maximum cross-correlation times (e.g., Abercrombie et al., 2017; Seo et al., 2022). Our approach is robust against uncertainties in source parameters arising from (1) an imprecise phase arrival time or/and (2) limited azimuthal station coverage. It is typically difficult to obtain precise phase arrival-time picks for earthquakes with complex ruptures involving small preceding subevents or interfering phases at a regional distance. Therefore, our proposed method can be highly useful to unravel source complexities of the 2021 M_w 4.9 Offshore Jeju Island earthquake that shows complicated source signals (Figure S1) and is recorded by stations in limited coverages (Figures 1a and 1b).

Figure S2 illustrates a construction of the origin-time preserved RSTFs and demonstrates how they work from the synthetic EGF waveform and synthetic target waveform that is generated with three subevents. The RSTFs are obtained by the following procedure: (i) pick the arrival time of the mainshock; (ii) by using the travel time of the mainshock obtained in (i), set the time window of the mainshock as well as the EGF waveforms that include seismic phases of interest (direct P or S wave; Lg wave) (Figure S2b); and (iii) perform the deconvolution to obtain RSTF. The EGF signals should be included in the same travel time window as the mainshock when the event occurred in close proximity to the mainshock, which is one basic criterion of selecting an EGF. In this procedure, the origin time differences between the EGF and target events are equally canceled out at every station, and thus a travel time difference can be represented as an offset time in RSTF.

In our study, we selected local RSTFs with variance reduction $\left(\left[1 - \frac{\sum_t (target(t) - EGF(t) * RSTF(t))^2}{\sum_t target(t)^2} \right] \times 100\% \right)$ greater than 80% for analyses for determining subevent locations and back-projection, and those RSTFs are presented in Figures 1c and d. The regional RSTFs with variance reduction greater than 60% (Figure 3b) are used to investigate slip distribution along strike.

Text S2. Implication of origin-time preserved RSTFs

In the case of the M_w 4.9 Offshore Jeju Island earthquake, we consider the mainshock rupture consisting of three subevents which include a small preceding subevent with 5% amplitude of subsequently following subevents (Figure S2a). As shown in Figure S2b, time windows that include P -wave source signals of the target event and EGF event can encompass any slight travel-time difference between the two events. A resulting RSTF, which is computed by aligning at P -wave arrival time, exactly starts from 0 s; origin-time preserved RSTF shows its start time to be shifted from 0 s (Figure S2c). Ideally, subevent locations can be determined by equation (1) in the main text regardless of any alignment approach; however, picking errors in phase arrival times can be mapped into the RSTF for

the case involving phase alignment. Location uncertainties can be further increased when *S* and *Lg* waves are used in estimating RSTFs because arrival times of such phases can be inaccurate as they are typically buried in the coda waves. If we use a time window that preserves the origin times of each event, we can effectively exclude the factor leading to uncertainty that could arise during the alignment of waveforms and incorporate more phases (*P* and *S* waves as well as *Lg* wave) when retrieving RSTFs.

The quality check of the obtained RSTFs can be done by examining whether their waveforms remain the same regardless of their temporal shift. Since deconvolution (a division in the frequency domain) is essentially the backward process of the circular convolution of two periodic functions, waveform alignment within the designated time window should only change a phase but hardly change the shape of RSTF. As demonstrated in Figure S3, our RSTF shapes remain unchanged regardless of shifting the origin time of the EGF event, unless its origin time is too uncertain that signals of both events cannot be included in the time window properly.

Text S3. Causal time adjustment of RSTF

We use projected Landweber deconvolution (Bertero et al., 1997) which constrains causality to RSTF, thus setting functions to be zero before 0 s. Since the RSTF does not exactly start from 0 s as described in Text S2, the causal function constraint is adjusted to involve two small subevents. For example, the start times of the RSTFs are before 0 s at stations UDO and CJD and after 0 s at MRD (Figures 1c and d). Specifically, the starting point of the causal time depends on the exact travel time difference between the mainshock and EGF, and if the EGF arrives earlier, the RSTF should start after 0 s, otherwise before 0 s.

The preceding small subevents are hardly discernable for *Lg*-wave waveforms at regional distances due to the high-frequency attenuation and coda-wave interference (Figure 3a). Then, the arrival time cannot be accurately determined. For this reason, we set the causal time generously so that functions can have non-zero values after about -0.1 s when retrieving *Lg*-wave RSTFs. Taking into account that small subevents are hardly resolvable, we only used the waveforms of the main rupture S1 and S2 for *Lg*-wave RSTF analysis.

Text S4. Relative moments between the mainshock subevents

We estimate the moment ratio of N1 and N2 using the peak amplitude ratio of the *P* wave relative to S1 at raw vertical-component velocity seismograms at local stations, of which signals are clear and not influenced by any signal processing (Figure S1). Using the relationship between velocity amplitude and moment with an assumption of self-similarity that is $\dot{u}(t) \propto M_0^{1/3}$, we determine the moment magnitude of small preceding events.

On the other hand, *Lg*-wave RSTFs are used to estimate the moment ratio between S1 and S2 because two pulses appear clearly at all observed azimuths. A relative moment ratio between target and EGF events can be estimated by summing the area under the RSTF waveform, which should be constant ideally regardless of station locations but may differ by as much as a factor of two depending

on the stations (Vallée, 2004). The area under the RSTF is represented by a sum of moment release from each subfault when we perform 1-D fault slip inversion. Therefore, normalized areas of S1 and S2 from the observed *Lg*-wave RSTFs are used as their moment ratio. We integrate the area of *Lg*-wave RSTF from the start time (Figure 3b, filled triangles) to the end time (Figure 3b, open triangles) for each subevent. Then, the moment ratio between S1 and S2 is obtained by the average ratio of the area between S1 and S2. The estimated moment ratio between S1 and S2 is 1:0.64.

The moment magnitude of each subevent (M_w in Table S1) is estimated by dividing the total moment of 2.58×10^{16} N m by the ratio between four subevents.

Text S5. Static shear stress perturbation analysis

We estimated stress perturbations induced by the nucleation events N1 and N2. We use a circular rupture model for the relationship between a stress drop ($\Delta\sigma$) and a source radius (r) (Eshelby, 1957).

$$\Delta\sigma = \frac{7}{16} \frac{M_0}{r^3} \quad [1]$$

The first nucleation event, N1, started at the deeper part of the rupture plane with a rupture duration of about 0.1 s that yielded a rupture of 0.12 km radius with assumption of rupture velocity of $0.7 \times V_s$ and stress drop of ~ 27 MPa with its seismic moment (1.04×10^{14} N m, Table S1) as depicted in Figure 2d. Then, the second nucleation event, N2, about 0.15 km shallower depth just off the N1 source, is triggered.

The source duration of N2 could not be estimated with confidence because it is tightly placed between N1 and S1. Assuming the self-similar rupture at constant stress drop for nucleation events (Beroza and Ellsworth, 1996), we have a source radius of ~ 0.16 km for N2 since it has a slightly greater seismic moment of 2.63×10^{14} N m than N1 (Table S1). N2 triggers the largest subevent S1 within a short time of ~ 0.1 s, as S1 lies close to it, as shown in Figure 2e (see Figure S1). The distances between subevents (N1-N2: 158 m; N2-S1: 224 m; see Table S1) are close to the estimated source radii of the subevents (N1: 120 m, N2: 160 m).

Based on Andrews (1980), we model the slip of subevents within the circular fault rupture and its static shear stress perturbation on the mainshock fault plane (e.g., Ellsworth and Bulut, 2018; Yoon et al., 2019). The Lamé constant μ and λ is assumed to be 30 GPa. While the stress transfer is calculated for the foreshock sequence in Ellsworth and Bulut (2018) and Yoon et al. (2019), we obtain stress transfer between subevents cascading during the nucleation process. The average slip D and slip distribution $d(r)$ on the circular fault of radius R ($r < R$) can be represented by the following equation:

$$d(r) = D \left[1 - \left(\frac{r}{R} \right)^2 \right]^{3/2} = \frac{M_0}{\mu \pi R^2} \left[1 - \left(\frac{r}{R} \right)^2 \right]^{3/2} \quad [2]$$

Text S6. Hypocenter locations and origin times of subevents by regional *Lg* RSTFs

The delayed origin time and horizontal hypocenter location from the EGF location, t_0 and x_0 , for subevents S1 and S2 can be determined by fitting azimuthally varying start time of each subevent in regional *Lg* RSTFs to the equation (1) in the main text by considering azimuth only (i.e., the horizontal take-off angle of 90°).

$$\tau_i(\phi_j) = \Delta t_i - \frac{D_i \cos(\phi_j)}{V_{P,S}} \quad [3]$$

In this case, θ_{ij} in the equation (1) in the main text is substituted by ϕ_j which is an azimuthal angle from strike direction to j -th station location, and D_i is a horizontal distance along the fault direction measured from the EGF location as reference point. To estimate the location (D_i) and delay of origin time (Δt_i) of subevents, the grid search is performed in intervals of 50 m spatially and 0.01 s temporally, then the best estimates for the hypocenter locations and origin times for S1 are -100 m (east) and 0.12 s, and for S2 are 600 m (west) and 0.80 s, respectively. The inter-hypocentral distance between S1 and S2 is similar to those obtained by local *P*- and *S*-wave RSTFs.

Text S7. Dispersion effect of *Lg* wave on RSTFs

We conducted analyses to assess the effect of *Lg* wave dispersion on RSTFs, especially in frequency range of 0.8–6 Hz. We stacked the envelopes of *Lg* waveforms recorded at stations in Korean Peninsula, which are filtered at 25 frequency bands between 0.2 and 10 Hz. Each envelope is plotted against the apparent group velocity (Figure S9a). The peak amplitude of each envelope at different frequency bands is marked as a colored square (Figures S9a and S9b). As Figures S9a and S9b show, the group velocities corresponding to the peak amplitudes in the frequency band of 0.8–6 Hz are in a range of 3.4–3.45 km/s (see red squares in the two figures). We then computed a relative peak amplitude ratio to the stacked envelope of raw waveform for various frequency bands (Figure S9c). Figure S9c shows that dominant energy is observed at the frequency band of 0.8–6 Hz (see red squares). We further estimated uncertainties to properly define a range of group velocities corresponding to significant amplitude levels. The group velocity ranges that correspond to 90% and 50% of the peak amplitude are shown as thick black and thin gray error bars, respectively, in Figure S9b. As this figure shows, in the frequency band of 0.8–6 Hz, both the 90% and 50% amplitude levels correspond to the group velocity ranges of 3.4–3.5 km/s and 3.1–3.6 km/s, respectively.

Next, we computed synthetic RSTFs to see how the RSTF waveforms vary at different group velocities, since the energy of *Lg* wave is mostly concentrated at the group velocity range of 3.1–3.6 km/s. We used 1-D slip inversion result (Figure 4a) as an input model to construct synthetic RSTF, which is $\widehat{\text{RSTF}}(t, v_g)$, where v_g is a group velocity of *Lg* wave. We note here that v_g is used instead of V_s in equation (3) in the main text for the forward modeling. The synthetic RSTF obtained from $v_g = 3.4$ km/s (i.e., $\widehat{\text{RSTF}}(t, 3.4 \text{ km/s})$) is compared with $\overline{\text{RSTF}}(t)$, which is the mean of $\text{RSTF}(t)$ computed by averaging $\widehat{\text{RSTF}}(t, v_g)$, where $v_g = 3.1\text{--}3.6$ km/s (Figure S10). The absolute error relative

to the area (defined by $|err| (%) = 100 \times \sum_t |\widehat{\text{RSTF}}(t, v_g) - \overline{\text{RSTF}}(t)| / \sum_t \overline{\text{RSTF}}(t)$) is up to 2.1%, and the variance reduction is greater than 99.9% along the fault strike for the $\widehat{\text{RSTF}}(t, 3.4 \text{ km/s})$. The shapes of $\widehat{\text{RSTF}}(t, v_g)$ are mostly affected when the rupture direction and wave propagation direction are parallel (strike direction at $AZ = 90\text{--}95^\circ$ in Figure S10). When both directions are orthogonal, there is no Doppler effect, resulting in an invariant $\widehat{\text{RSTF}}(t, v_g) = \text{STF}(t)$ ($AZ = 0\text{--}5^\circ$ in Figure S10).

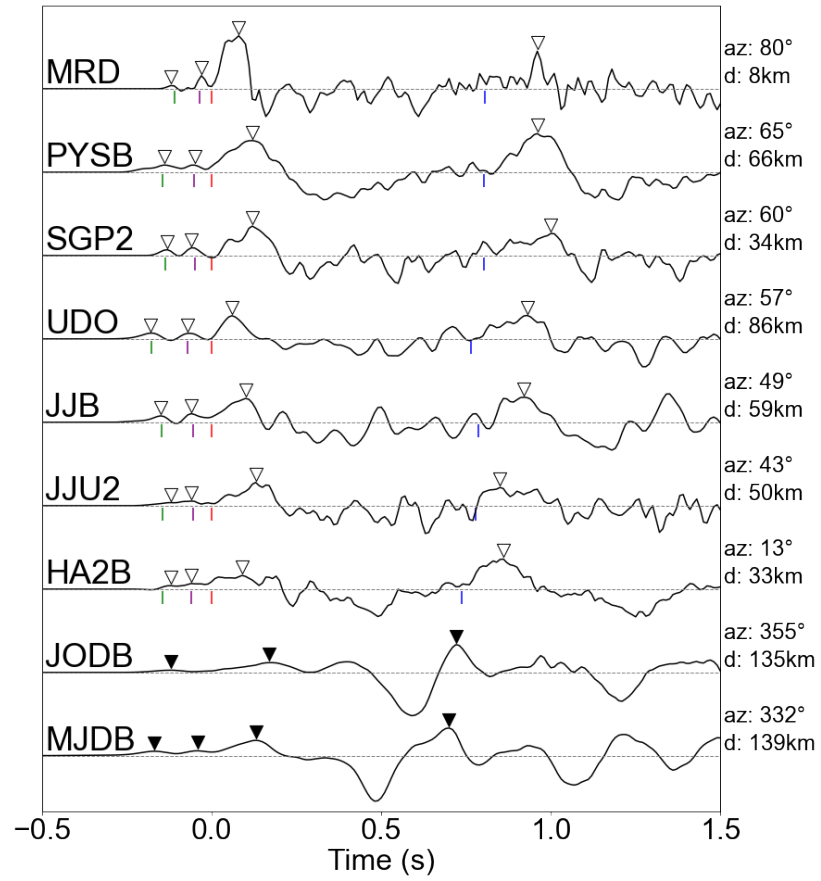


Figure S1. Raw vertical records of the M_w 4.9 mainshock at broadband stations within the distance of 140 km, plotted according to azimuth. P -wave peaks for four subevents are indicated by inverted triangles. Traces with open inverted triangles are plotted with polarity reversed for ease of comparison. The green, purple, red, and blue ticks indicate predicted arrival times at each station based on the determined origin time and hypocenter location of subevents N1, N2, S1, and S2, respectively.

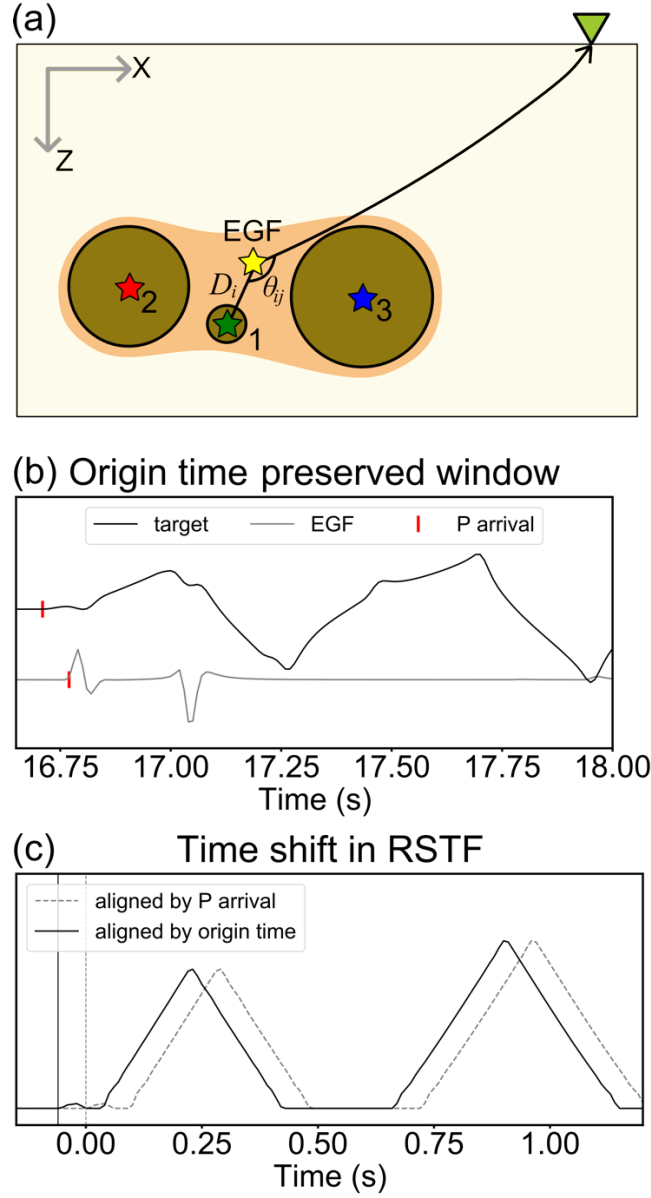


Figure S2. (a) Schematic figure showing hypocenters of three sequential slip patches of subevents (1, 2, and 3 indicated as green, red, and blue stars, respectively) and EGF (yellow star). θ_{ij} is an angle between ray direction of the j -th station and the i -th subevent location from the EGF. D_i is a distance of each i -th subevent ($i=1, 2$, and 3) from the EGF. (b) Origin-time preserved window. Synthetic waveforms of a target event and EGF around the arrival time of P wave at a distance of 100 km and azimuth of 315° . Source durations are 0.1 s, 0.4 s, and 0.5 s; relative origin times are -0.05 s, 0.1 s, and 0.6 s; and relative amplitudes are 1, 20, and 25 for three subevents, respectively. (c) Comparison between origin-time preserved RSTF and RSTF computed by aligning at P -wave arrival time.

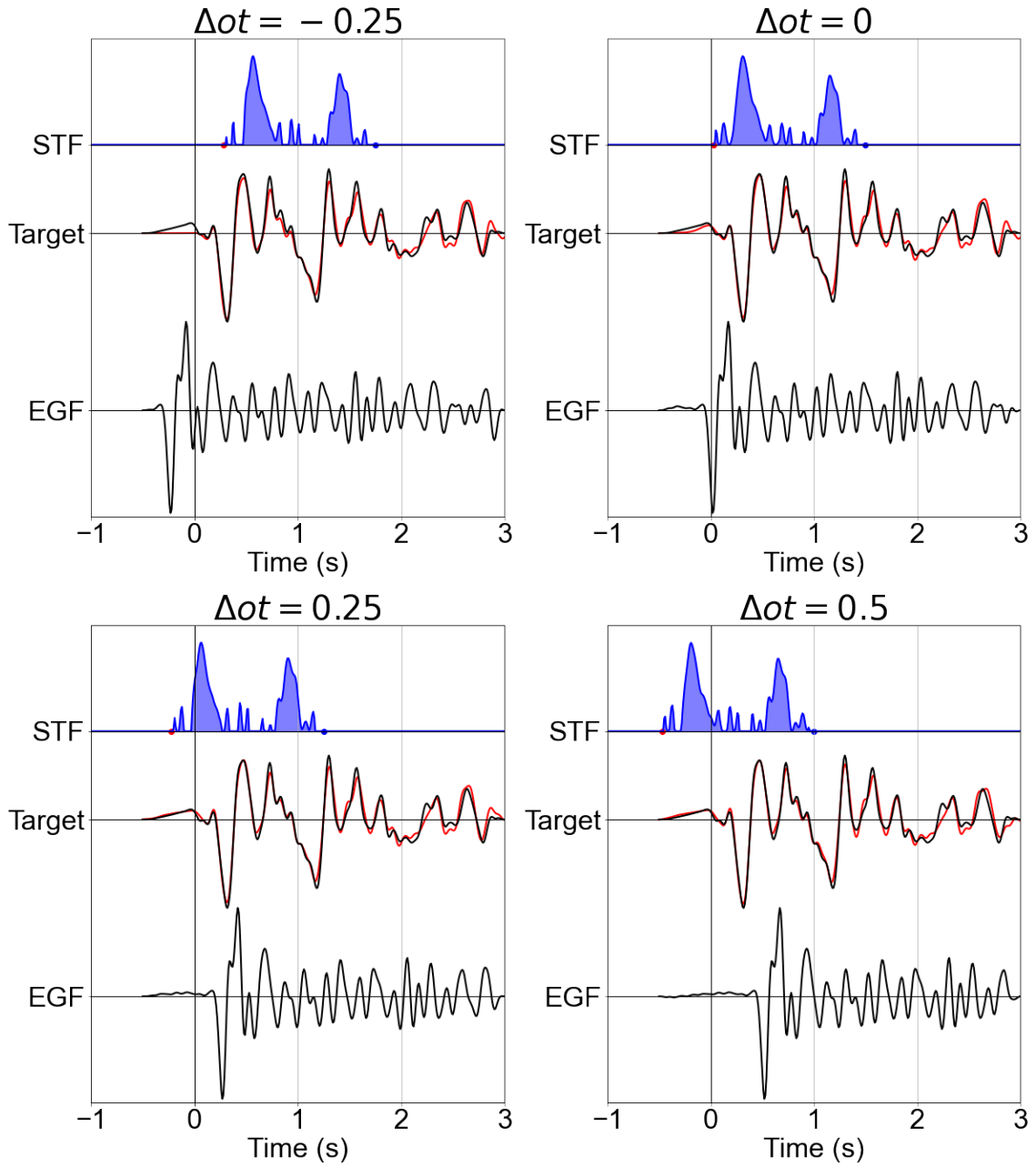


Figure S3. Calculation of RSTFs at station SGP using *P* wave by adding origin time error (Δot) of -0.25, 0, 0.25, and 0.5 s. Reconstruction of the target (mainshock) waveforms, which is a convolution of RSTF and EGF waveforms, is represented by red line. The origin time error of EGF or target event can cause a time shift in the RSTFs but hardly change a shape of RSTFs. The overall shape is maintained given that time window is long enough to contain main source signals.

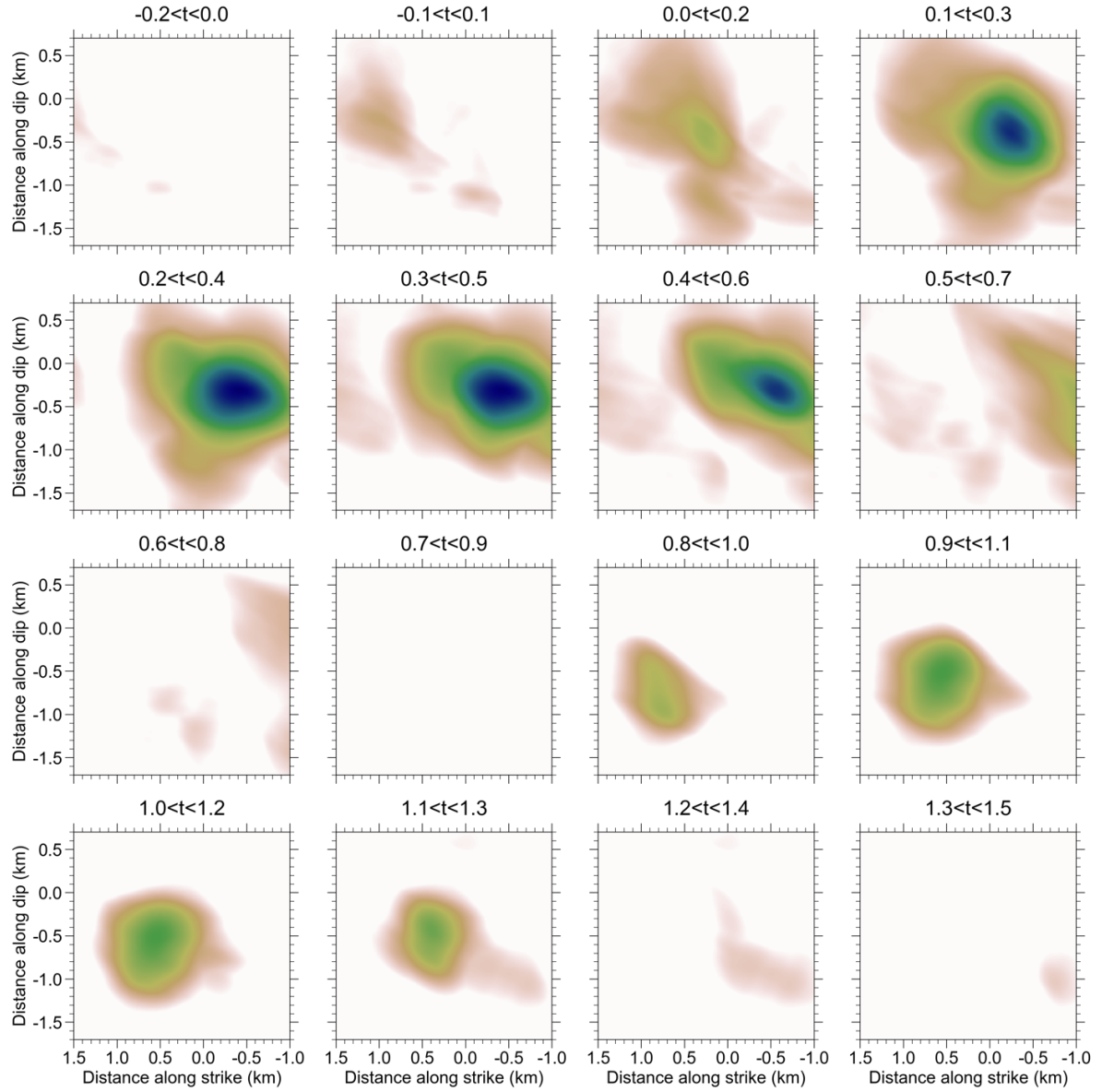


Figure S4. Snapshots from the back-projection of local RSTFs with a time interval of 0.1 s. Each snapshot shows maximum beam power for 0.2 s duration. Two bright spots are imaged at 0.3 s and at 1.0 s, which indicate rupture area of subevents S1 and S2, respectively.

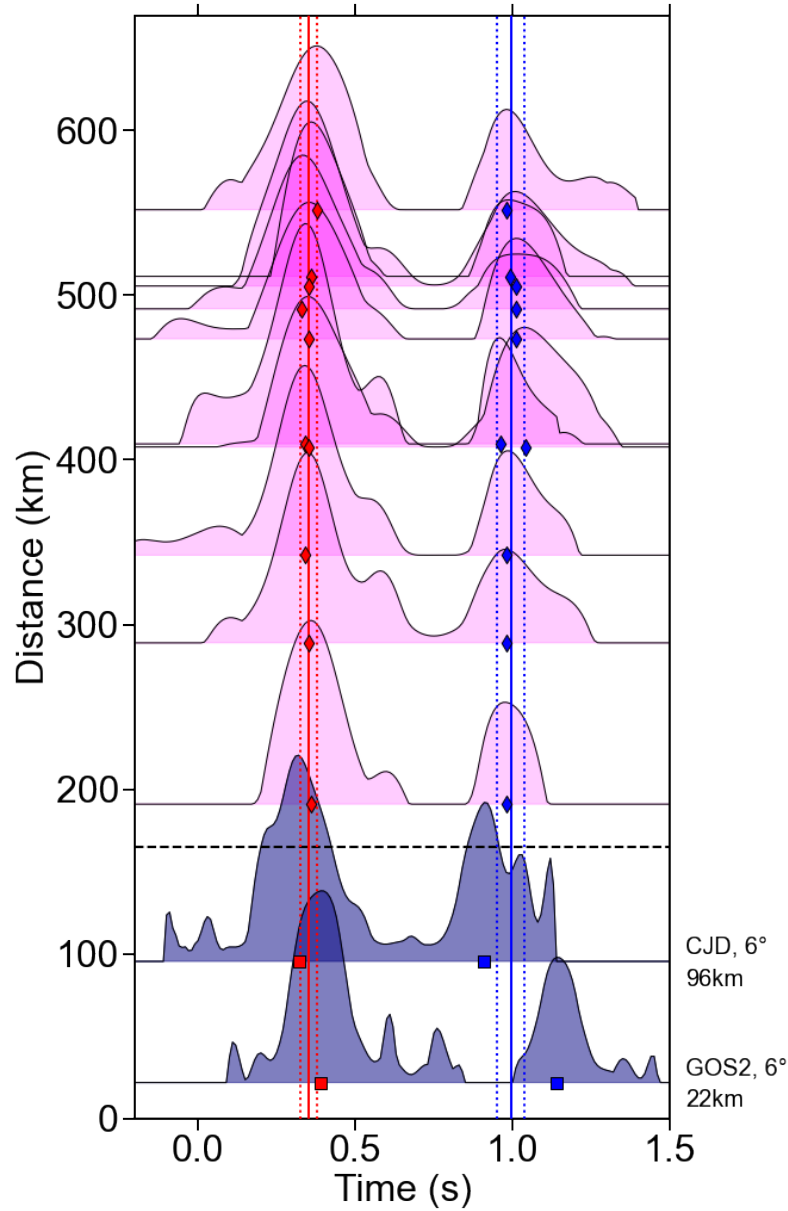


Figure S5. Variation of RSTF waveforms along the epicentral distance. The plot shows individual RSTFs in a 10-degree azimuth bin ($AZ=0^{\circ}-10^{\circ}$) retrieved at a local (navy) and regional (magenta) distance. RSTFs at a local distance (GOS2 and CJD) are processed identically to regional RSTFs to satisfy the equivalent condition. Vertical red and blue solid lines mark the mean peak times of S1 and S2, respectively, for distances greater than 165 km (black dashed line). Vertical dotted lines indicate two standard deviations. The peak times of S1 and S2 for the distance greater than (or less than) 165 km are indicated by red and blue diamonds (or squares), respectively.

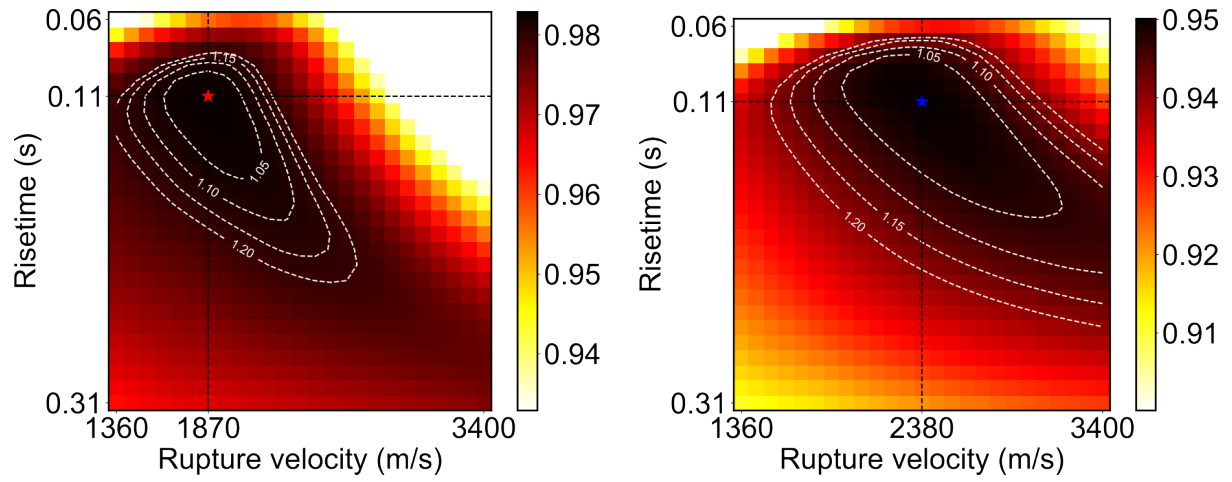


Figure S6. 1-D fault-slip inversion of subevents S1 and S2 using regional *Lg*-wave RSTFs to search for optimal rupture velocity and risetime. Variance reductions of inversion for S1 (left) and S2 (right), respectively, when rupture velocity and risetime are varied. Optimal rupture velocities which maximize variance reduction at a risetime of 0.11 s are indicated by red and blue stars for S1 and S2, respectively. The trade-off between rupture velocity and risetime is observed. It is clear that S1 shows a slower rupture velocity than S2, which corresponds to a relatively lower variability of duration along the azimuth range in *Lg*-wave RSTFs (Figure S7a). The relative misfit ratio (mean square error) to the optimum value is indicated by the contour of white dashed lines.

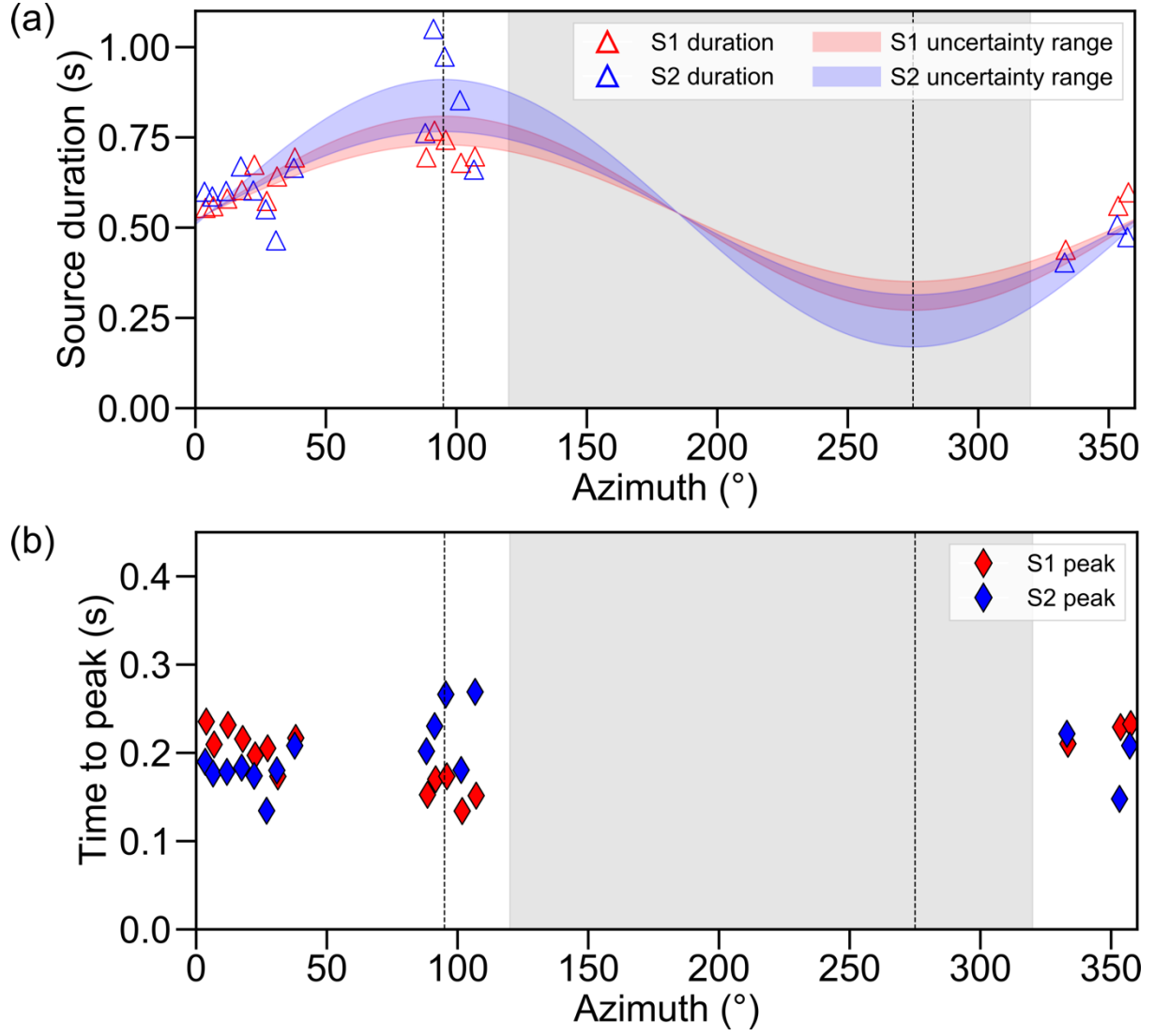


Figure S7. (a) Source durations and (b) times to peak of subevents S1 (red) and S2 (blue). Azimuth range with no data is shaded in gray. The black dashed vertical lines represent the fault strike directions. Markers and colors are the same as in Figure 3b. Transparent red and blue areas indicate the uncertainty range of azimuthal variation of apparent source duration ($\tau(\varphi_i) = t_r + \frac{L}{V_R} - \frac{L}{V_S} \cos \varphi_i$) for S1 and S2, respectively, according to rupture velocities (V_R) and risetimes (t_r), which are selected within 1.1 times of the optimum misfit contour line in Figure S6. In this case, the fixed source duration of 0.54 s is used to calculate rupture length (L) of S1 and S2. Less azimuthal variability in S1 indicates a slower rupture velocity. Decrease in time to peak appears in the strike direction (95°) only for S1.

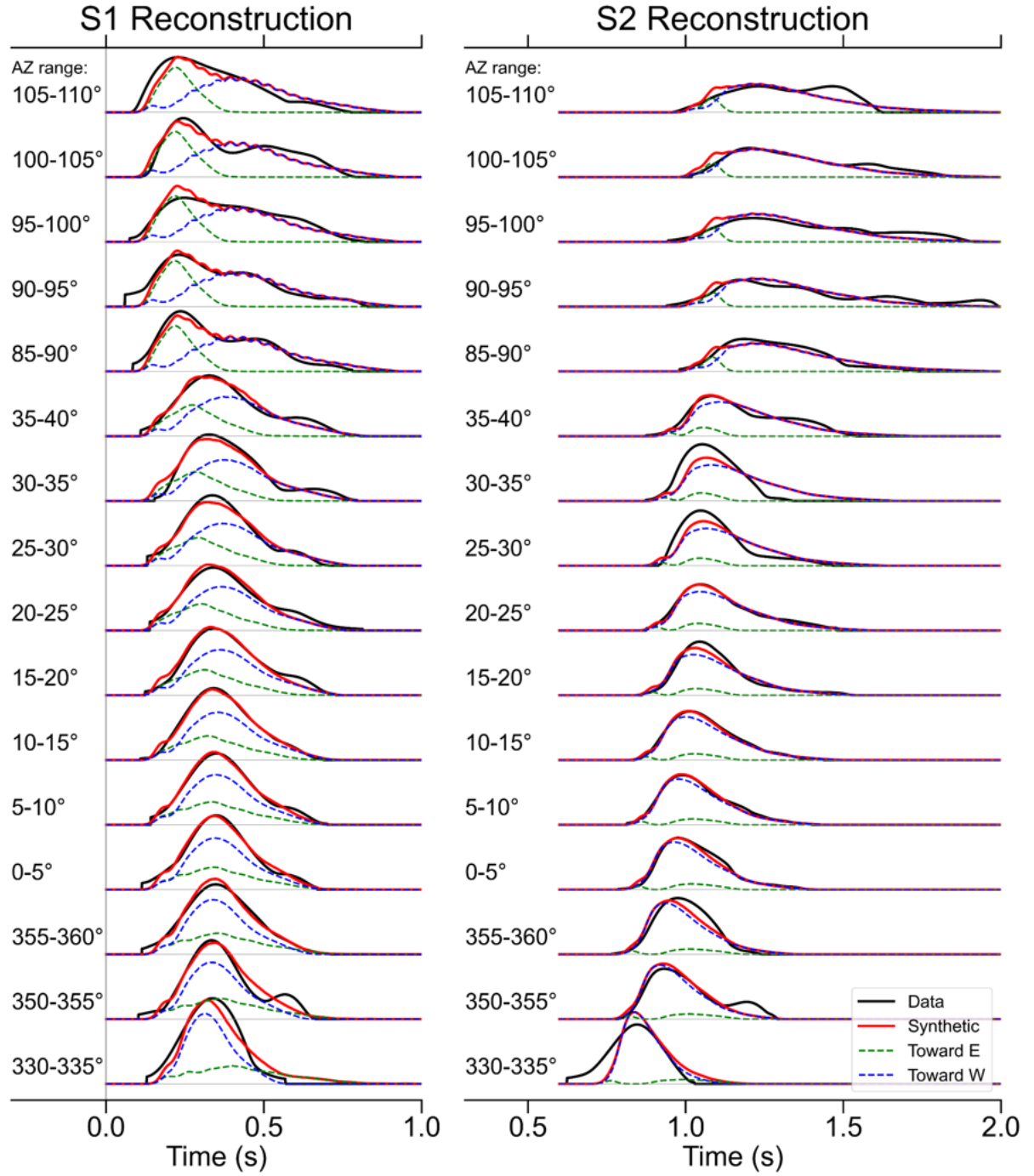


Figure S8. Comparison between the *Lg* RSTFs (black) and synthetic RSTFs (red) calculated by forward modeling of 1-D fault slip inversion results for S1 (left) and S2 (right). The ruptures toward east and west are represented by green and blue dashed line, respectively. The eastward rupture (green dashed line) accounts for the total moment release of 33% for S1 rupture, but RSTFs of S2 rupture are well represented by the westward rupture alone (blue dashed line).

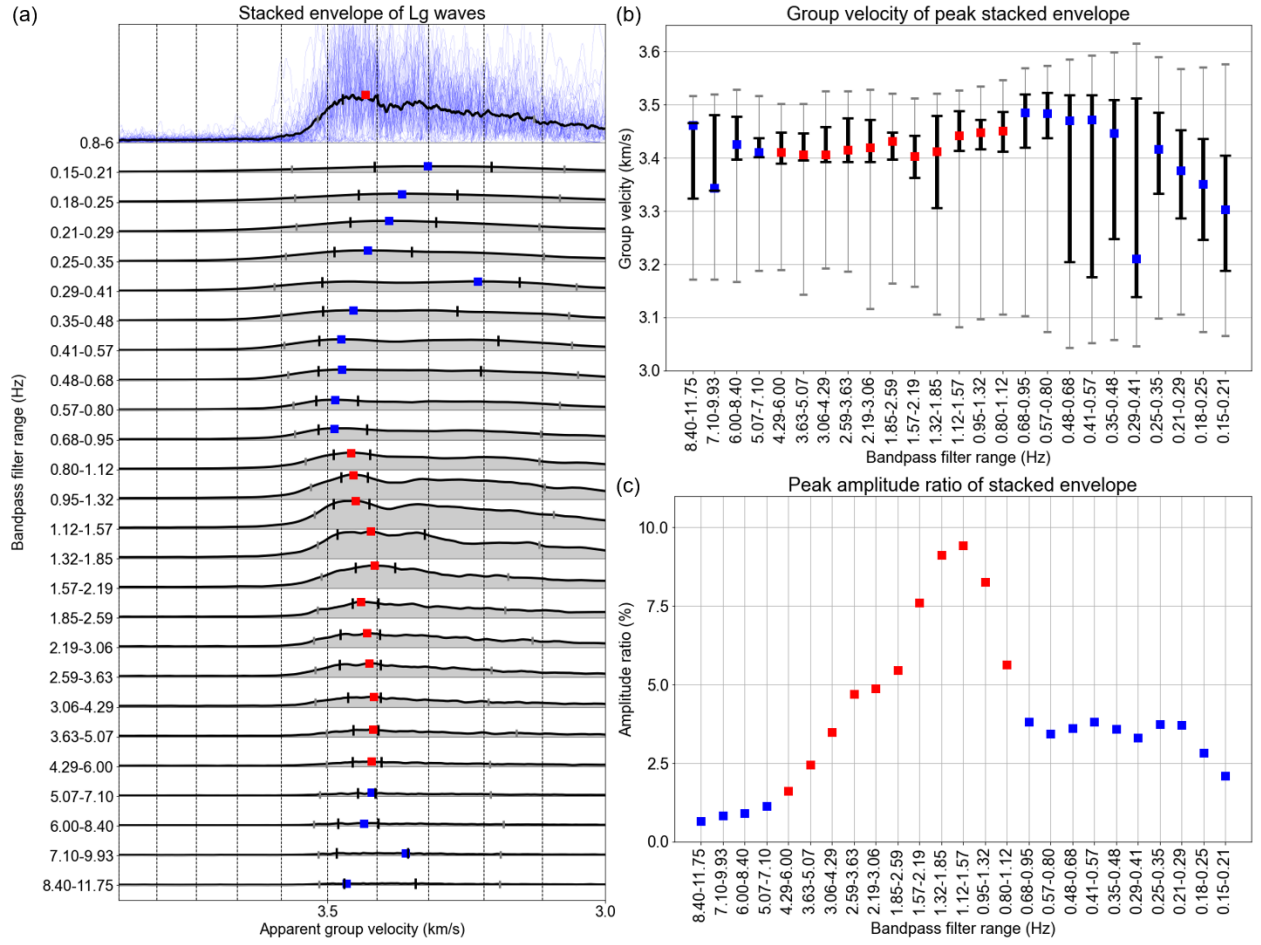


Figure S9. (a) Dispersion curve of *Lg* waves plotted against apparent group velocity of 4.0 – 3.0 km/s. The envelopes of bandpass-filtered waveforms are stacked at each frequency range and represented as black solid lines. Individual and stacked envelopes of traces filtered at the frequency band of 0.8 – 6 Hz are shown as blue and black lines, respectively, at the top of the figure. A peak amplitude of each envelope is indicated as a square marker in red if the frequency range is within the 0.8 – 6 Hz band and blue otherwise. (b) Group velocity corresponding to the peak envelope amplitude with uncertainty estimate. The 90% and 50% of the peak amplitude are shown as thick black and thin gray error bars, respectively. (c) A relative peak amplitude ratio between the stacked envelope and the raw waveform for various frequency bands.

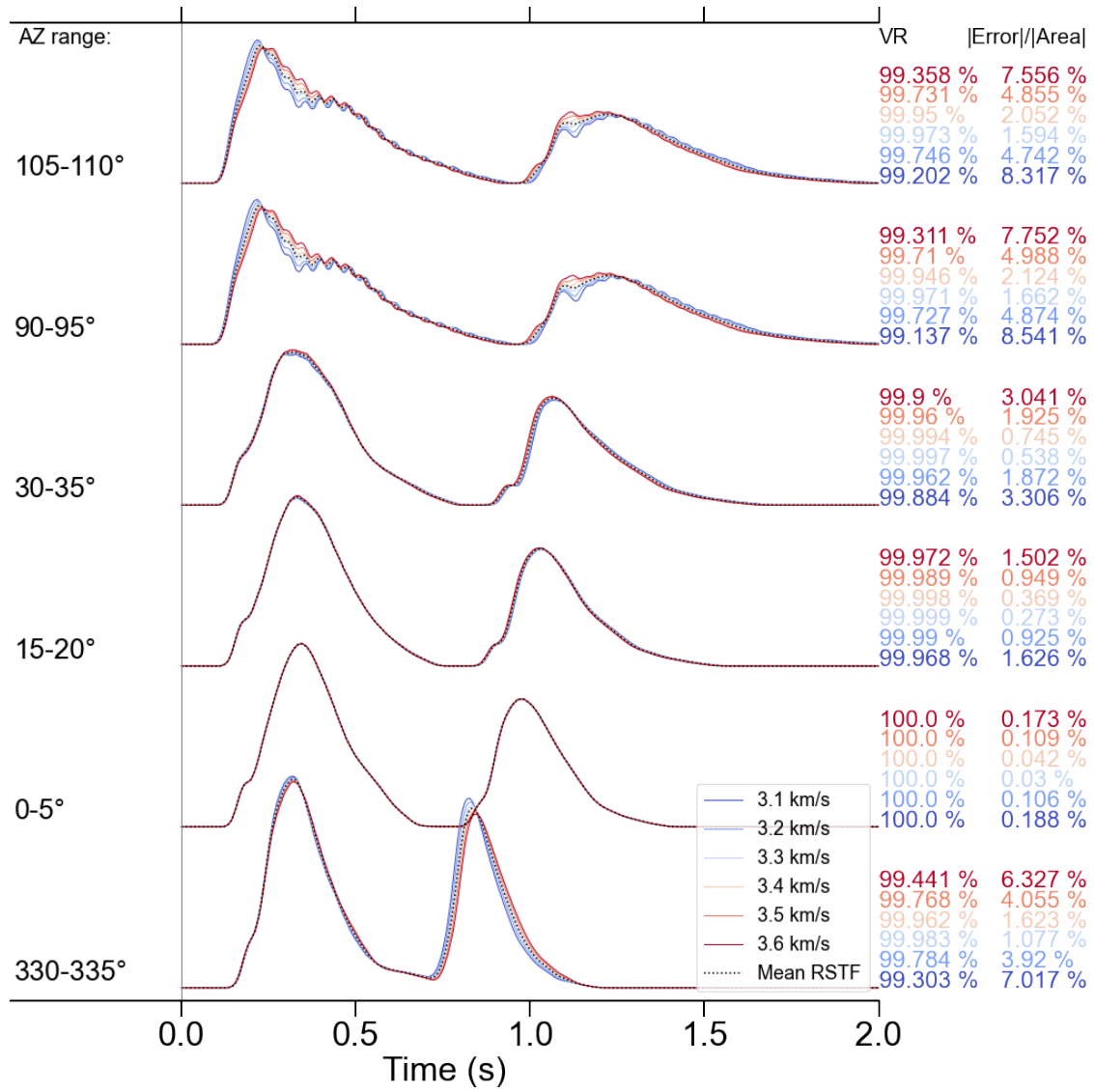


Figure S10. Synthetic $\widehat{\mathbf{RSTF}}(t, \mathbf{v}_g)$ computed at different azimuth directions. The synthetics are calculated by varying the group velocity from 3.1 to 3.6 km/s at a 0.1 km/s interval. Each $\widehat{\mathbf{RSTF}}(t, \mathbf{v}_g)$ at different group velocity is plotted with different colors. $\widehat{\mathbf{RSTF}}(t)$ is indicated as a black dotted line. The absolute error ($|err|$) and the variance reduction (VR) estimated at each group velocity relative to $\widehat{\mathbf{RSTF}}(t)$ are shown on the right side of the plot.

	ID	Origin Time	M_w	x (m)	y (m)	dx (m)	dy (m)
0	EGF	2021-12-15 06:06:47.00	2.87	0	0	-	-
1	N1	2021-12-14 08:19:14.52	3.31	-200	-850	125	125
2	N2	2021-12-14 08:19:14.61	3.58	-150	-700	100	100
3	S1	2021-12-14 08:19:14.68	4.76	-250	-500	75	100
4	S2	2021-12-14 08:19:15.39	4.63	350	-800	225	225

Table S1. Hypocenter locations relative to EGF location on the fault plane, origin times, and estimated moment magnitudes of four subevents. The dx and dy are location errors along strike and dip directions, respectively, corresponding to 25% misfit perturbation.